Publication Year	2015
Acceptance in OA	2020-04-15T14:27:01Z
Title	Medicina array demonstrator: calibration and radiation pattern characterization using a UAV-mounted radio-frequency source
Authors	PUPILLO, Giuseppe, NALDI, Giovanni, BIANCHI, GERMANO, MATTANA, Andrea, MONARI, JADER, PERINI, FEDERICO, POLONI, MARCO, SCHIAFFINO, MARCO, BOLLI, Pietro, Lingua, A., Aicardi, I., Bendea, H., Maschio, P., Piras, M., Virone, G., Paonessa, F., Farooqui, Z., Tibaldi, A., Addamo, G., Peverini, O. A., Tascone, R., Wijnholds, S. J.
Publisher's version (DOI)	10.1007/s10686-015-9456-z
Handle	http://hdl.handle.net/20.500.12386/24051
Journal	EXPERIMENTAL ASTRONOMY
Volume	39

Medicina Array Demonstrator: Calibration and Radiation Pattern Characterization Using a UAV-Mounted Radio-Frequency Source

G. Pupillo, G. Naldi, G. Bianchi, A. Mattana, J. Monari, F. Perini, M. Poloni, M. Schiaffino

INAF - Istituto di Radioastronomia, Bologna, Italy

P. Bolli[*]

INAF - Osservatorio Astrofisico di Arcetri, Florence, Italy

Tel. +39 055 2752214, Fax: +39 055 220039, E-mail: pbolli@arcetri.inaf.it

A. Lingua, I. Aicardi, H. Bendea, P. Maschio, M. Piras

Politecnico di Torino - Dipartimento di Ingegneria dell'Ambiente, del Territorio e delle Infrastrutture, Torino, Italy

G. Virone, F. Paonessa, Z. Farooqui, A. Tibaldi, G. Addamo, O.A. Peverini, R. Tascone

CNR - Istituto di Elettronica e di Ingegneria dell'Informazione e delle Telecomunicazioni, Torino, Italy

S. J. Wijnholds

Netherlands Institute for Radio Astronomy, Dwingeloo, The Netherlands

Abstract: One of the most challenging aspects of the new-generation Low-Frequency Aperture Array (LFAA) radio telescopes is instrument calibration. The operational LOw-Frequency ARray (LOFAR) instrument and the future LFAA element of the Square Kilometre Array (SKA) require advanced calibration techniques to reach the expected outstanding performance. In this framework, a small array, called Medicina Array Demonstrator (MAD), has been designed and installed in Italy to provide a test bench for antenna characterization and calibration techniques based on a flying artificial test source. A radio-frequency tone is transmitted through a dipole antenna mounted on a micro Unmanned Aerial Vehicle (UAV) (hexacopter) and received by each element of the array. A modern digital FPGA-based back-end is responsible for both data-acquisition and data-reduction. A simple amplitude and phase equalization algorithm is exploited for array calibration owing to the high stability and accuracy of the developed artificial test source. Both the measured embedded element patterns and calibrated array patterns are found to be in good agreement with the simulated data. The successful measurement campaign has demonstrated that a UAV-mounted test source provides a means to accurately validate and calibrate the full-polarized response of an antenna/array in operating conditions, including consequently effects like mutual coupling between the array elements and contribution of the environment to the antenna patterns. A similar system can therefore find a future application in the SKA-LFAA context.

Keywords*: Aperture arrays; Square Kilometre Array; calibration techniques; antenna pattern; antenna measurements.*

---

[*] Corresponding author

1 INTRODUCTION

The radio astronomical community is currently working on the detailed design for the Square Kilometre Array [1,2]. The National Institute for Astrophysics (INAF) has been involved in this effort since 2005, with particular emphasis on the aperture array developments. Currently, the INAF-IRA is deeply involved in the Aperture Array Design and Construction (AADC) consortium aimed to develop the hardware parts of the Low-Frequency Aperture Array element of the SKA. Low frequency instruments such as LOFAR [3] and the SKA-LFAA require advanced calibration and instrument characterization techniques, taking into account effects like mutual coupling between array elements and environmental effects, to reach their expected performance. Of particular interest is the characterization of the directional response of the instrument as function of frequency, which is one of the key issues during the commissioning of any radio telescope. This information is required to make adequate primary beam corrections. In this paper, we demonstrate that a flying test source mounted on an Unmanned Aerial Vehicle can be successfully used to establish the directional response in full polarization of the individual antennas in the array as well as to perform calibration of the array of the antennas.

The Medicina Array Demonstrator is one of the technological research side-projects funded by INAF in 2013 in the context of their SKA contribution. This 3x3 aperture array implements, on a much smaller scale, a receiving chain similar to the one of a SKA-LFAA station. The main goals of the MAD project are: *(i)* testing the analog receiver chain in a realistic environment, *(ii)* implementing the digital signal processing algorithms like beam-forming, and *(iii)* calibrating and characterizing the array in its operative conditions (e.g., on the ground, with mutual coupling effects, etc.) using a novel procedure based on an artificial source. The latter consists of a micro-UAV flying in the far-field region of the Antenna Under Test (AUT). For a small array like MAD, the flying height of the UAV satisfies the far-field condition for both the single antenna element and the array as a whole. For larger arrays (such as a LOFAR station or a SKA-LFAA station), a reduced subset of antennas should be considered to assure the far-field condition. This approach will require the development of proper criteria to propagate the calibration from the sub-arrays to the whole station. Compared to other methods [4], this approach is an efficient and low-cost solution for characterizing antenna or array patterns for systems whose dimensions are not compatible with anechoic chambers and including also the effects due to the real operative environment. Another important aspect of the proposed system consists of having a controlled test source available for initial calibration during the commissioning phase of the instrument. This opens up a plethora of options, such as antenna position calibration, which could allow for large cost savings in roll-out owing to the much lower placement accuracy requirement needed for the antenna positions. Finally, the experimental data can be also used to validate the electromagnetic model, which can then be applied for further and more complex numerical analysis. All the mentioned features of this system gives us a valuable tool for validation and characterization of the antenna arrays envisaged for the SKA.

Previous works on the UAV system [5,6] have shown excellent results for single antenna pattern measurements in the frequency range between 150 and 408 MHz. This paper reports on successful calibration and characterization of an array pattern instead, which was achieved during the campaign performed in May 2014 with the UAV-system at 408 MHz.

This paper is organized as follows: Section 2 describes the MAD architecture. Section 3 briefly shows the main features of the hexacopter system and the flying strategies. The experimental results for the embedded element patterns are reported in Section 4.1 whereas both the calibration strategy and the simulated and measured array patterns are discussed in Section 4.2. Finally, Section 5 draws the conclusion and indicates future activities.

2 MEDICINA ARRAY DEMONSTRATOR

The Medicina Array Demonstrator is a 3x3 regularly spaced array arranged in a rhomboidal configuration (see Fig. 1) installed on the premises of the Medicina radio astronomical station (30 km East of Bologna, Italy). This location allows the utilization of the station infrastructure and the already installed BEST-2 receiving chains (with optical fiber links) [7]. The operating frequency was chosen around 408 MHz to exploit the existing infrastructures and also because of the protection given by the national frequency plan to the frequency band 406.1 – 410 MHz. The legal protection at 408 MHz, the possibility to use a sufficiently high transmitted power level and the usage of a well-designed receiving system with good spectral selectivity avoided any problem related to Radio Frequency Interferences.

The antennas were deployed directly on the ground without any metallic ground plane underneath and with a minimum inter-element spacing equal to 1.5 m. The array configuration without ground plane was selected in order to provide a more cost-effective solution for the SKA-LFAA, and the antenna has been optimized accordingly. The antenna polarizations are aligned along the cardinal directions. A photogrammetry measurement with the camera placed on the hexacopter was performed [8] in order to accurately measure (with mm-accuracy) the real positions of the centers of each antenna. The antenna alignment towards the cardinal directions and the verticality were instead measured using a different topographic instrument (total station).

The array elements are Vivaldi antennas operating in dual-linear polarization [9], which were designed by the Italian team and proposed as a candidate for the antennas of the SKA-LFAA element [10]. This Vivaldi antenna covers the frequency range from 70 to 450 MHz with a matching level that has been designed to provide a sky noise limited system ($|S_{11}|$ lower than -5 dB up to 200 MHz and lower than -10 dB above 200 MHz). The two-fold symmetry of the antenna geometry gives a remarkable isolation between the two orthogonally polarized channels (better than 45 dB) and very low cross-polarization levels on the principal planes (lower than -35 dB) from zenith direction to 45 degrees. Additionally, the antenna shows an approximate sky-coverage of 45 degree from zenith i.e. total sensitivity drop (Stokes I parameter) within 3 dB, which is consistent with the SKA-LFAA requirements [10].

Each of the two output ports of the array elements is connected to a 50 Ω single-ended Low Noise Amplifier (LNA) with good noise performance, better than 30 K from 100 to 400 MHz, and high dynamic range (OIP3 > +30 dBm). After the LNA, an analog RF-to-Optical converter transmits the signal through a single-mode optical fiber, which is a technology candidate for potential use in SKA-LFAA. The active components of the front-end (LNA and optical transmitter) are powered by batteries with a life-time of 17 hours. The front-end and the batteries are packaged inside the antenna thickness thus obtaining an easily deployable structure with an optical output. A further advantage for using batteries is to avoid copper cables laid on the ground to power the active stages, therefore reducing the electromagnetic perturbation to the antenna response.

The optical links transmit the received signals to a shielded and temperature-controlled environment inside the Medicina station where a second part of the receiver is housed. Here, the signal is converted back to the RF domain by optical receivers and down-converted by a mixing system to a 16 MHz IF band, centered around 30 MHz. Each chain also features band filter shaping and digitally controlled attenuators to perform analogue signal equalization [11].

After that, the signals are digitized by the ADC board (64 inputs, 12 bit) at 40 MHz and then transmitted to a ROACH-1[†] CASPER[‡] back-end based on a XILINX VIRTEX-5 FPGA. The digital back-end is responsible for forming the array beam for both polarizations and for calculating the correlation products needed for the estimation (calibration) of the complex receiver path gains. The first block of the back-end processing system is the frequency channelization stage, which is realized by a Fast Fourier Transform-based Polyphase Filter Bank. An adjustable complex gain equalizer performs the amplitude and phase corrections before quantization. The correlator multiplies and averages the output signals of antenna pairs selected from a proper subset of non-redundant baselines only. Additionally, it simultaneously provides the auto-correlations of all antennas, which can be used to measure the embedded element power pattern. The beam-former module works in parallel with the correlator and it calculates the weighted sum of the complex antenna signals for the two linear polarizations separately. These outputs are the calibrated beams of the two polarizations.

[†] Reconfigurable Open Architecture Computing Hardware (https://casper.berkeley.edu/wiki/ROACH)

[‡] Collaboration for Astronomy Signal Processing and Electronics Research (https://casper.berkeley.edu/)

Fig. 1 – Pictures of MAD with optical fibers aligned in NS direction. Left: side-view. Right: aerial view (this figure has been processed to include cardinal directions and antenna labels).

3 HEXACOPTER SYSTEM AND FLIGHT STRATEGIES

The micro-UAV (hexacopter), shown in Fig. 2, is equipped with a continuous-wave RF signal generator based on a Phase-Locked Loop synthesizer (ADF4350) operating from 137.5 MHz up to 4.4 GHz, with a maximum power level ranging between +5 and +8 dBm. Two telescopic monopoles are connected to the generator with an integrated broadband balun (Minicircuits ADTL1-12). The total dipole length (326 mm) is selected to obtain a good impedance matching at the unbalanced port of the balun at 408 MHz. A full-wave electromagnetic simulation of the test source was performed with CST Microwave Studio for characterizing the source pattern.

The hexacopter is a custom product manufactured by an Italian company on the basis of our specifications. The six arms are made of aluminum and are about 70 cm long. The length of the rotor blades is about 30 cm. The heart of the hexacopter is the control board Mikrokopter KGPS ver. 1.0 equipped with the u-blox 6S sensor. This system allows for an arbitrary GNSS (Global Navigation Satellite System)-controlled autonomous flight with a maximum duration of about 15 minutes. However, a remote pilot is needed for the takeoff and landing operations. The same control board has a built-in Inertial Measurement Unit (IMU), which provides a measurement of the three orientation angles (bearing, pitch, and roll) with an accuracy of about 2 degrees for all of them. The telemetry link is based on X-bee modules operating at 2.4 GHz, the radio control is working at 35 MHz.

One of the innovative features adopted in the MAD campaign is the tracking of the UAV position with a dual-frequency GNSS receiver, also located on the hexacopter. This system, which exploits a differential cinematic technique, replaces the more complex system based on the total station [6]. A ground GNSS station is also located in the proximity of the AUT.

In this paper, a selection of the most significant flights out of the more than 20 performed during the campaign is chosen to show the relevant experimental results. The measurements are identified by an ID code as reported in Table 1. Two flight strategies were used for the measurements: a stationary flight at zenith (for amplitude and phase equalization/calibration) and a planar quasi-rectilinear scan (centered at zenith) along one of the antenna principal planes (for both embedded element and array beam pattern measurements). Some of the quasi-rectilinear scans, i.e., flights 6 and 7, are performed twice, with opposite direction, for data redundancy.

The relative orientation of the source dipole with respect to the AUT on the ground corresponds to the bearing angle of the UAV, which can be set as a variable of the flying path. The reported flights are performed with the transmitting antenna aligned along the NS direction, corresponding to the co-polar orientation of the array elements aligned in the same direction. Similar results have been obtained for the elements which pertain to the other polarization.

All trajectories have a constant height from the ground, large enough (100 m) to fulfill the far-field condition both for the array and for the single antennas, the far-field region $(2\frac{D^2}{\lambda})$ being equal to 55 m, where $D = 4.5\ m$ represents the maximum extent of the array. The maximum distance from the zenith position during the rectilinear trajectories is equal to 100 m, in order to reach a scanning angle range of ±45 degrees.

An example of the trajectory measured with the dual-frequency GNSS system along the NS direction (flight 6) is plotted in Fig. 3(a). The three plots give the real hexacopter displacements along NS and EW directions with respect to the position of the array center, as well as the height above the ground. The orthogonal displacement with respect to the ideal trajectory is up to 2 m in EW direction and up to 5 m in the height. Additionally, Fig. 3(b) shows the three orientation (Euler) angles recorded by the onboard IMU. Bearing and roll are always below 4 degrees, whereas pitch ranges up to 9 degrees due to the high wind conditions.

Flight ID code	Back-end acquisition starting date/time [UTC]	Trajectory (ENU) [m]	Tx antenna alignment	Speed [m/s]
1	22/05/2014, 10:30:14	Stationary at zenith: (0,0,100)	NS	0
2	22/05/2014, 10:34:02	Stationary at zenith: (0,0,100)	NS	0
3	22/05/2014, 16:05:04	Rectilinear from S to N (0,-100,100) → (0,100,100)	NS	1.5
4	23/05/2014, 07:25:01	Stationary at zenith: (0,0,100)	NS	0
5	23/05/2014, 07:33:34	Rectilinear from N to S (0,100,100) → (0,-100,100)	NS	1.5
6	23/05/2014, 08:13:36	Rectilinear from N to S (0,100,100) → (0,-100,100)	NS	1.5
7	23/05/2014, 08:15:38	Rectilinear from S to N (0,-100,100) → (0,100,100)	NS	1.5
8	23/05/2014, 08:18:12	Rectilinear from W to E (-100,0,100) → (100,0,100)	NS	1.5
9	23/05/2014, 08:45:46	Stationary at zenith: (0,0,100)	NS	0

Tab. 1 – Details of the hexacopter flights mentioned in the paper.

Fig. 2 – Foreground: hexacopter equipped with RF transmitter and telescopic dipole. Background: cylindrical reflector antenna of the Northern Cross Radio Telescope.

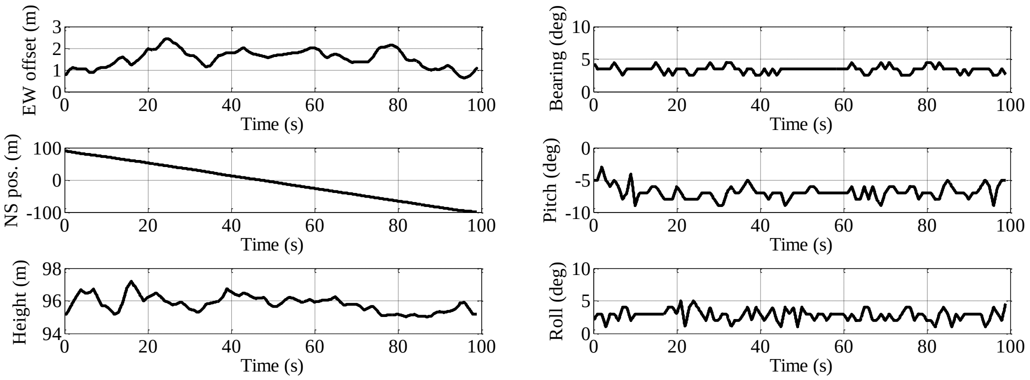

(a) (b)

Fig. 3 – UAV position (a) and orientation (b) versus time during flight 6.

4 CALIBRATION AND EXPERIMENTAL RESULTS

The radiation patterns reported in this section have been extracted from the recorded output signals of either the various element RF chains or the beam-former system. Indeed, these output signals are not only proportional to the AUT (antenna element or array) patterns. They are instead also related to: source power, radiation pattern of the transmitting antenna, free-space path loss and receiver gain [5]. Nevertheless, all these effects have been removed from the acquired data using the extraction procedure reported in [6]. Such a procedure exploits both the hexacopter position and orientation data discussed in Section III to determine the actual source contribution impinging on the AUT during each instant of the flight. A general block diagram of the main components of the set-up is shown in Fig. 4. The same figure also shows the quantities that are considered to evaluate the final experimental antenna pattern. Only the data pertaining to one polarization (oriented NS) will be discussed. However, similar results were obtained for the EW one. The main experimental settings of the transmitting and receiving systems adopted during the measurements are summarized in Table 2.

All the measured data are compared to the numerical simulations obtained from CST Microwave Studio, where the AUT geometry is placed over a finite ground plane representing the soil (permittivity and conductivity values equal to 8 and 0.06 S/m, respectively). The electromagnetic model does not include any additional metallic element, since the antennas are connected to the receivers through optical fibers. The simulations of the AUT patterns are computed in the far-field region, therefore neglecting the electromagnetic coupling between the AUT and the transmitting antenna.

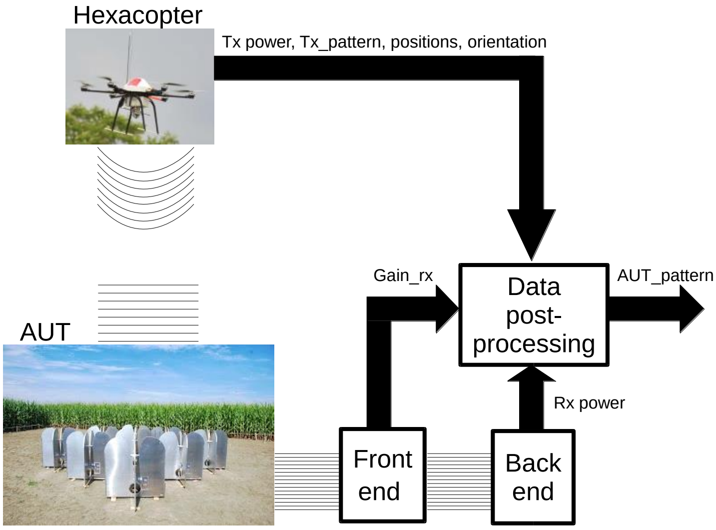

Fig. 4 – Block scheme of the set-up. The antenna on board of the hexacopter transmits a radio wave, which is received by the antennas, conditioned by the analog front-end and finally acquired in the back-end (see the thin lines for the signal path). The data-processing to obtain the measured AUT pattern is performed starting from the received power measured by the back-end (Rx power) and taking into account the transmitting antenna pattern (Tx pattern), the source power set in the PLL synthesizer (Tx power), the measured hexacopter position and orientation and finally the front-end gain (see the thick black lines which represent the data flow).

Element	*Characteristic*	*Value*
Hexacopter	Continuous-wave frequency	408 MHz
	Power source level	+5 dBm
	Tx antenna gain (0 - 45 deg)	6 - 0 dBi
	Flying height	100 m
	Free-space path loss (0 - 45 deg)	64 - 68 dB
	Polarization	Linear, oriented North-South
Antenna element and Front-end	Vivaldi antenna gain (0 - 45 deg)	7 - 2 dBi
	LNA gain	22.4 dB
	Noise figure of the LNA	0.44 dB
	Receiver (including LNA) gain	45 dB
	Noise figure of the receiver	18.5 dB
Back-end	Input bandwidth	20 MHz
	Integration time	From 51.2 μs to 0.06 s
	ADC sampling precision	12 bit
	Output channel bandwidth	19.5 KHz
	Input dynamic range	[-30 : +10] dBm
	Time resolution	51.2 μs
	FFT channels	1024
	Correlator data rate	11.25 Mb/s
	Beam-former data rate	1.25 Mb/s
	Output data quantization	32 bit (complex)

Tab. 2 – Summary of the settings for the MAD experimental measurements.

4.1 Embedded antenna patterns

The digital back-end acquires simultaneously the RF signals received by the nine array elements. Therefore, all the embedded-element patterns are measured within a single hexacopter flight. The embedded co-polar patterns for all the elements are plotted in Figs. 5 and 6 for the *E*-plane (NS direction, flight 7) and *H*-plane (EW direction, flight 8) respectively. As expected, each element shows a different embedded pattern due to its different position in the array.

The agreement between measurements and simulations is remarkable (always better than 1 dB), especially for the *E*-plane. The *H*-plane, which is broader than *E*-plane for the adopted Vivaldi element at 408 MHz, is in fact more critical as far as simulation is concerned, owing to the finite size of the dielectric ground (the truncation edges in the model are more illuminated). The fast ripple present in some patterns is produced by scattering sources in the proximity of the array, like the Northern Cross Radio Telescope.

The symmetrically placed antennas, such as antennas #2 and #6 in the *E*-plane or antennas #2 and #4 in the *H*-plane, should provide identical patterns. However, there are some discrepancies mainly due to their different height from the ground, which was not completely flat. It should be pointed out that such deformations of the ground were also introduced in the simulations, which show similar discrepancies for the symmetrical antennas. In other words, the terrain effect is visible both in experimental and theoretical data. This confirms the validity of the explanation reported above. The sensitivity of the pattern with respect to the antenna distance from ground, which will be also visible in Fig. 10, is due to a quite significant back-lobe of the Vivaldi antenna and is related to the antenna wide sky-coverage and limited size at these low-frequencies. This effect was already known from simulations and it has been carefully verified with the developed measurement system as well, showing the importance of in-situ antenna measurements. Finally, it should be pointed out that future versions of the Vivaldi antenna will have a mitigated sensitivity with respect to ground [12].

Another reason for the small discrepancies between the performance of the symmetrically placed antennas is related to the real trajectory of the hexacopter, which can be a few meters away from the ideal principal planes i.e. *E*-plane and *H*-plane. This fact is due to the limited accuracy of the navigation board of the UAV, which is based on single-frequency GPS. Nevertheless, the real hexacopter position is measured using an on-board dual-frequency differential GNSS system, which provides a centrimetric accuracy (an error of 2 cm at 100 m lead to an angular error of 0.01 degrees). This information is used to simulate the AUT pattern along the real flying path of the hexacopter. In this way, measurement and simulations can be compared along the same trajectory. Therefore, the small differences between *E*-plane of antennas #2 and #6 and *H*-plane of antennas #2 and #4 can be appreciated in both measurement and simulation.

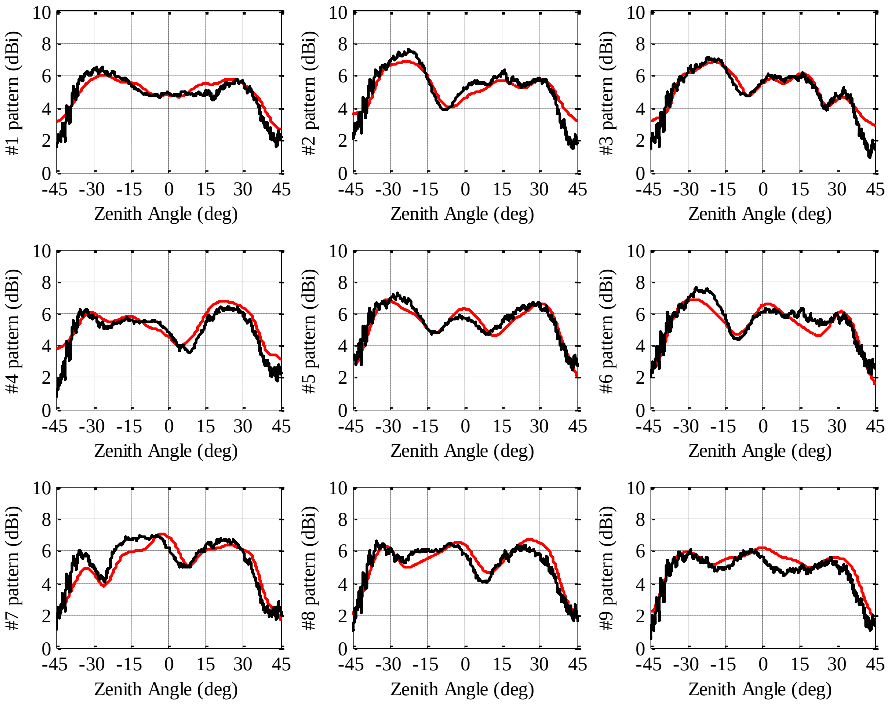

Fig. 5 – Measured (black) and simulated (red) embedded co-polar patterns in *E*-plane.

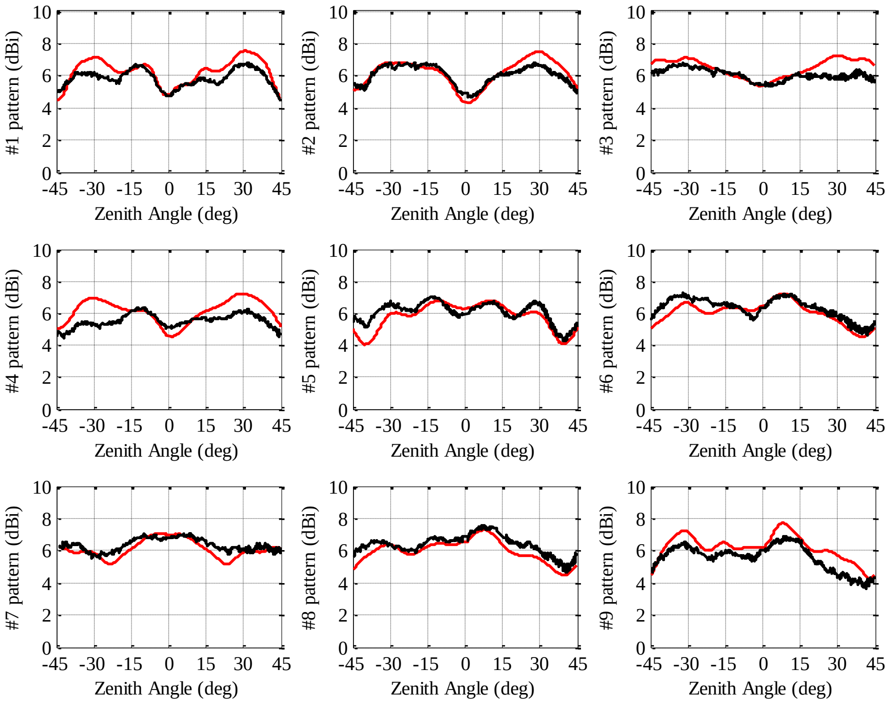

Fig. 6 – Measured (black) and simulated (red) embedded co-polar patterns in *H*-plane.

The measured patterns shown in Figs. 5 and 6 were computed by taking into account the real orientation of the hexacopter during the flight (measured by the onboard IMU). It is interesting to compare the extracted measured pattern for the central element (#5) with and without such a correction. This latter case implies that, with respect to the procedure described in Fig. 4, the orientation information of the hexacopter is not included in the final data processing. The plot in Fig. 7(a) shows the beneficial effects of the UAV orientation correction on the extracted pattern. This pattern has been measured with flight 6, which was affected by high wind and whose trajectory is shown in Fig. 3. The high pitch angle of the UAV creates a distortion of the extracted pattern. This effect is more apparent in the *E*-plane, where the transmitter antenna pattern is narrower and hence more sensitive to the orientation angle. As evident from Fig. 7(b) where the differences between the two sets of measurement data and the simulated results are plotted, the corrected data show a remarkable improvement, from 2.5 to 1 dB, as far as the agreement between measurement and simulation is concerned.

Finally, data repeatability has also been investigated. In particular, the embedded pattern of the central element has been measured several times in different days, see Fig. 8(a). The agreement among the different curves in Fig. 8(b) turns out to be very good: less than 0.5 dB in the elevation range between -30 to 30 degree (a part for a narrow spurious reaching 1 dB at around +15 degree of the elevation angle). Outside this range, differences increases up to 1.5 dB due to both the lower antenna directivity and the presence of the fast ripple mentioned above.

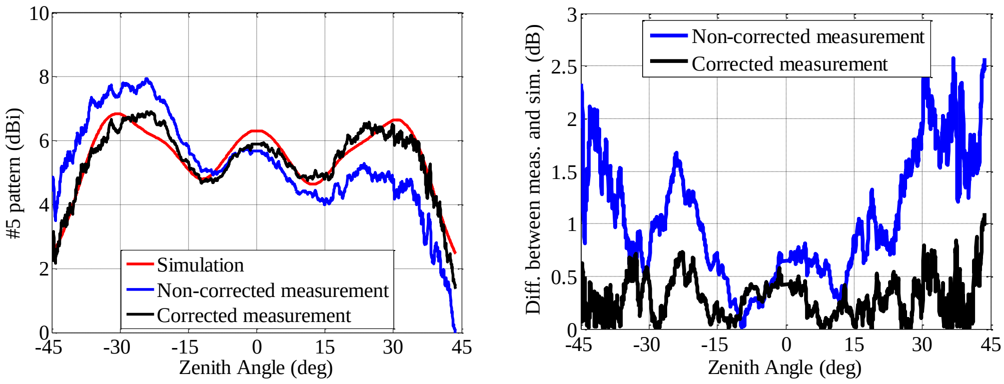

(a) (b)

Fig. 7 – (a) UAV orientation correction (flight 6): simulation (red); non-corrected pattern (blue); corrected pattern (black). (b) Absolute value of the discrepancy between measurements and simulation: non-corrected pattern (blue); corrected pattern (black).

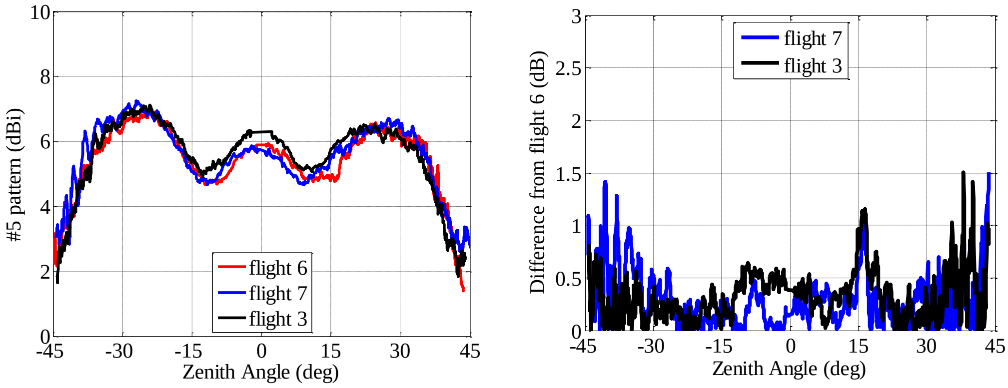

(a) (b)

Fig. 8 – (a) Embedded patterns repeatability for three different flights: 3 (black), 6 (red) and 7 (blue). (b) Absolute value of the discrepancy between the patterns for different flights: difference of flight 7 from flight 6 (blue); flight 3 from flight 6 (black).

4.2 Array calibration and array beam patterns

The array beam is formed by combining the signals received by all elements with appropriate amplitude factors and time delays. In particular, the beam forming technique is applied once the systematic errors produced by the spurious variations of phase and amplitude between the array elements (e.g. differences in the electronic gains and different signal paths in the receiving chains) are corrected. The process of measuring and applying the phase and amplitude corrections is called calibration. In the MAD experiment, all the calibration tasks have been carried out with the hexacopter stationary at zenith at a nominal height of 100 meters.

First of all, preliminary coarse automatic analogue signal power equalization is performed to ensure that the back-end is working in its linear regime. Afterwards, the magnitude of the digital calibration coefficients is calculated from the auto-correlations in order to achieve the same received power at zenith.

As far as the phase of the digital calibration coefficients is concerned, such parameters are computed as the opposite of the measured instrumental phase shifts of each array element (φ_j). For each polarization, one antenna is used as reference: element #7 was selected for the NS polarization. For element *#j*, the digital back-end computes the complex cross-correlation product R_j of the received signals $V_j(t)$ with respect to the reference signal $V_7(t)$: $R_j = \langle V_7(t) V_j^*(t) \rangle$, where the superscript * denotes the complex conjugate. The measured phase is given by:

$$\phi_j = arctan\left(\frac{Imag(R_j)}{Real(R_j)}\right). \tag{1}$$

This value can be considered, in first approximation, as the sum of two terms:

$$\phi_j = \varphi_j + \omega\tau_g, \tag{2}$$

where φ_j is the unknown relative instrumental phase shift (due to cables, receivers, electronics, etc.) of the $\#j$ element, $\omega = 2\pi f$ is the signal angular frequency and τ_g is the geometric delay of the signal received from the element $\#j$ with respect to the reference *#7*. The latter is calculated, at a given time, from the array element coordinates and the hexacopter instantaneous position (measured by the differential GNSS receiver) as:

$$\tau_g = \frac{r_j - r_7}{c}, \tag{3}$$

where r_7 and r_j are the distances from element #7 and *#j* to the hexacopter, respectively, and c is the speed of light. The final relative instrumental phase shifts φ_j are obtained by substituting (1) and (3) into (2).

In order to increase the accuracy of the phase calibration, the correction coefficients are estimated from the averaged correlator samples. The relative instrumental phase shifts and RMS computed from the correlator samples (integration time 51.2 μs) recorded during different stationary flights are listed in Table 3. These values were computed from the whole set of samples recorded during each stationary flight. The number of considered samples spans from 3.4×10^5 (flight 2) to 1.3×10^6 (flight 9) depending on the specific flight. The data in Table 3 confirm both the good repeatability of the phase measurements and the phase stability of the receiving chains. Some discrepancies in the phase measurements could be further reduced, for instance, by including the hexacopter orientation angles in the calibration algorithm (here not considered) as well as by increasing the sampling rate of the hexacopter position (here set to 1 Hz). Since the first MAD digital back-end was limited to perform only few cross-correlations, we used the minimum number of baselines necessary to calculate the calibration parameters. The new version of the back-end, already successfully employed in the last part of the MAD campaign, allows the acquisition of the full correlation matrix. Therefore, we plan in the next campaigns to use all the $N(N-1)/2$ independent baselines to obtain a more accurate system calibration through use of an over-constrained estimator. Moreover, systematic errors can be investigated through the phase closure triangles.

Antenna ID	***Flights***							
	1		***2***		***4***		***9***	
	Phase	RMS	Phase	RMS	Phase	RMS	Phase	RMS
#1	276.8	0.9	276.5	0.5	273.4	2.3	279.2	1.1
#2	227.2	0.6	230.0	0.5	225.7	2.2	226.1	1.2
#3	233.4	0.7	236.3	0.5	233.8	2.5	232.8	1.7
#4	92.9	1.5	95.2	1.1	94.3	4.3	93.6	3.1
#5	358.29	0.6	1.3	0.4	347.5	1.4	350.3	0.9
#6	163.3	1.1	166.7	0.5	162.2	2.1	158.2	1.5
#7	0	0	0	0	0	0	0	0
#8	13.3	1.5	15.8	1.1	13.7	4.7	7.7	3.1
#9	36.5	1.1	39.6	0.8	41.3	2.2	30.3	1.4

Tab. 3 – Relative instrumental phases φ_j and RMS in degrees calculated for different flights.

The variations of the geometric delay along a proper hexacopter trajectory, conceived to maximize its effect over the selected baselines, will produce the characteristic interference fringes at the output of the correlator. Such interference fringes can be used to verify the array calibration in different directions after the complex coefficients are uploaded to the digital back-end. Figure 9(a) shows the normalized fringes for the eight baselines (#1 - #7, #2 - #7 …… #9 - #7) without phase correction, as function of the geometric delay, obtained with the hexacopter flying in the NS trajectory (flight

5). The fringe patterns after the phase calibration (using the coefficients calculated from the phase shifts of Table 3) are instead shown in Fig. 9(b) (flight 3).

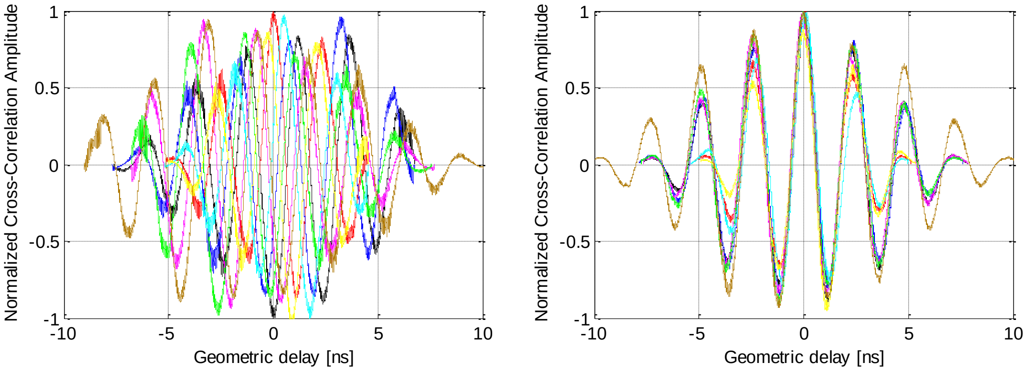

(a) (b)

Fig. 9 – Normalized fringe patterns for the NS trajectory: (a) before and (b) after phase calibration.

After the calibration procedure, the main fringe maxima of each baseline (geometric delay equal to zero) are well aligned in the direction of the calibration source (zenith) as clearly shown in Fig. 9(b). Some secondary maxima exhibit small but noticeable misalignments, revealing a direction-dependent effect in the relative antenna phase shifts. This phase direction-effect is caused by the mutual coupling between the array elements that produces a different phase pattern for each element, depending on both the array configuration and the element position within the array. This effect is highlighted in Fig. 10, where measured and simulated phase difference between elements #3 and #7 are plotted for flight 3, as a function of the zenith angle. The simulations were repeated for different distances between antennas and terrain, which represents indeed a critical parameter. Although some discrepancies are present, meaning that the simulation needs more refinement especially in the soil distance, a good agreement is already obtained.

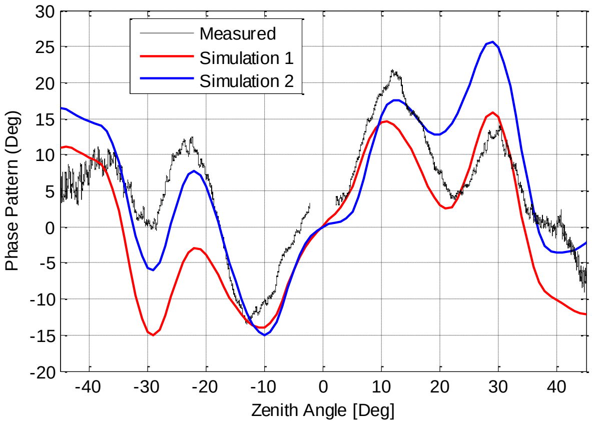

Fig. 10 - Comparison between the measured phase pattern obtained for baseline #3 - #7 (black line) and simulations considering a ground distance of 5 cm for both elements (red line) or 5 cm for antenna #3 and 10 cm for antenna #7 (blue line).

As a final result of the MAD campaign, Fig. 11 shows the measured and simulated array co-polar patterns in *E*- and *H*-planes. Such data have been collected during the same flights used for the embedded element patterns in Figs. 5 and 6. The system shows a very good dynamic range and the overall agreement is remarkable. The presence of grating lobes is due to the regularity of the array. There are some discrepancies in the secondary lobes and some occasional offsets (also in the main beam), which are due to both modeling and calibration inaccuracies. As mentioned in Section 4.1, the array elements are quite sensitive to their distance from ground, which was not completely flat. Such an effect has been modeled in the simulations, nevertheless some residual error is still visible.

Second, the significant phase variations along the zenith angle (see Fig. 10) has not yet been included in the calibration model. Such variations would be carefully investigated and accounted for in the next versions of the proposed calibration strategy.

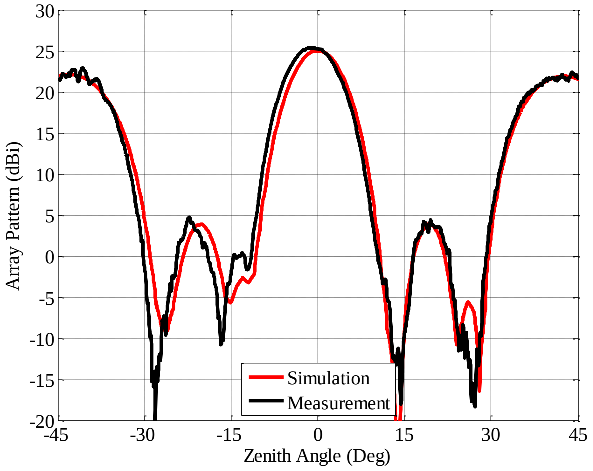

(a)

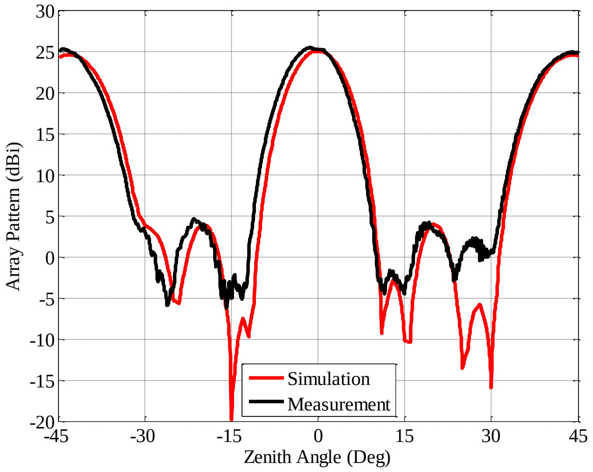

(b)

Fig. 11 – Experimental array patterns (black) compared to simulations (red): (a) *E*-plane (flight 7), *H*-plane (flight 8).

5 CONCLUSIONS AND FUTURE ACTIVITIES

A very promising approach for the initial calibration of a Low-Frequency Aperture Array has been implemented and tested on a small array installed in Medicina (Italy). The system is based on a UAV (hexacopter), which has been carefully modified to transport radio-frequency components. Specific care has been addressed to the mechanical symmetry of the hexacopter to avoid spurious cross-polarized contributions. Experimental results at 408 MHz show its applicability for measuring embedded element patterns as well as for calibrating the array and measuring its beam pattern. In more recent measurement campaigns, the frequency range of the system has already been extended from 50 to 650 MHz.

As a next step, we aim to apply the technique to a new Italian aperture array demonstrator called Sardinia Array Demonstrator composed of a significantly larger number (128) of Vivaldi antennas [13] and to one of the LOFAR stations. The latter consists of an 85-m diameter irregular array of low band antennas and a 40-m diameter regular array of high band antennas [3]. These arrays will represent a more appropriate test-bed for a single station of a large array like SKA-LFAA.

In the meantime, further technical upgrades are planned to be applied to the system such as performing cross-polarization measurements, improving the accuracy in the orientation angles, making the measurement process more automatic and transmitting a wide-band white noise signal or a comb-like signal. The latter is particularly valuable allowing simultaneous multi-frequency measurements and therefore reducing the measurement time. Naturally, this would imply transmitting radio-frequency signals in not-allocated bands and consequently specific authorizations are required from national administrations dealing with regulatory communication services.

The UAV based measurements of the embedded element patterns (in magnitude and phase) have demonstrated to be very effective to refine and validate the electromagnetic models. These improved models could be fundamental to achieve the high calibration accuracy required by SKA-LFAA and by the next generation wide field arrays. As already stated in Section 1, a fundamental aspect to be further investigated is the case of the hexacopter located in the far-field region of each individual antennas (or of a sub-station) but not in that of the whole station which has to be calibrated. This will be indeed the case for the larger SKA-LFAA stations, which are also characterized by a lower operative frequency range. Therefore, novel techniques to deal with such big stations should be investigated either on the basis of several properly-combined lower-order calibrations on predefined sub-arrays or defining calibration strategies with the UAV in the near-field region. The measurement we plan to perform to LOFAR will represent indeed a preparatory step for a future possible application to SKA.

References

[1] Dewdney, P.E., Hall, P.J., Schilizzi, R.T., and Lazio, T.J.L.W., “The Square Kilometre Array”, Proceedings of the IEEE, vol. 97, no. 8, pp. 1482-1496 (2009).

[2] Dewdney, P. E.: SKA1 System baseline design, (2013) http://www.skatelescope.org/wp-content/uploads/2012/07/SKA-TEL-SKO-DD-001-1_BaselineDesign1.pdf

[3] Van Haarlem, M. P., et al., “LOFAR: The Low Frequency Array”, Astronomy & Astrophysics, vol. 556, no. A2, pp. 1-53 (2013) DOI: 10.1051/0004-6361/201220873.

[4] Raucy, C., et al., “Low-cost near field pattern measurement technique for aperture array characterization,” in Proc. EuCAP, Goteborg, Sweden, pp. 661–665 (2013).

[5] Virone, G., et al., “Antenna Pattern Verification System Based on a Micro Unmanned Aerial Vehicle (UAV)”, IEEE Antennas and Wireless Propagation Letters, vol. 13 (2014).

[6] Virone, G., et al., “Antenna pattern measurements with a flying far field source (hexacopter),” Proceedings of CAMA 2014, Antibes Juan-les-Pins, France (2014).

[7] Bolli, P., et al., “Basic Element for Square Kilometre Array Training (BEST): Evaluation of the Antenna Noise Temperature”, IEEE Antennas and Propagation Magazine, vol. 50, no. 2, pp. 58-65 (2008), DOI: 10.1109/MAP.2008.4562257.

[8] Chiabrando, F., Lingua, A., Piras, M., “Direct photogrammetry using UAV: tests and first results,” ISPRS Archives, vol. XL-1/W2, pp. 81 86, UAV g2013, Rostock, Germany (2013).

[9] Monari, J.et al. “Aperture Array for Low Frequency: the Vivaldi solution”, International Conference on Electromagnetics in Advanced Applications (ICEAA), Turin, Italy (2013).

[10] Bij de Vaate, J. G., et al., “Low frequency aperture array developments for phase 1 SKA,” Proceedings URSI, Istanbul, Turkey (2011).

[11] Perini, F., Bianchi, G., Schiaffino, M., Monari, J., “BEST receiver experience: general architecture, design and integration”, Wide Field Science and Technology for the Square Kilometre Array, Proceedings of the SKADS Conference, Chateau de Limelette, Belgium (2009).

[12] Tibaldi, A., et al., Design considerations for a low-frequency Vivaldi array element, PIERS Proceedings, pp. 240 - 244, Stockholm (2013).

[13] Murgia, M., et al., "Sardinia aperture array demonstrator," SPIE 9145, Ground-based and Airborne Telescopes V, 91454S (2014), DOI: 10.1117/12.2055793.